Pyroelectric waste heat energy harvesting using the Olsen cycle on Pb(Zr, Ti)O$_3$-Pb(Ni, Nb)O$_3$ ceramics

An-Shen Siao,[1,2] Ian M. McKinley,[1] Ching-Kong Chao,[2] Chun-Ching Hsiao,[3,4] and Laurent Pilon[1,a)]

[1]*Mechanical and Aerospace Engineering Department, Henry Samueli School of Engineering and Applied Science, University of California - Los Angeles, Los Angeles, California 90095, USA*
[2]*Department of Mechanical Engineering, National Taiwan University of Science and Technology, Taipei 10607, Taiwan*
[3]*Smart Machine and Intelligent Manufacturing Research Center, National Formosa University, Yunlin County 63201, Taiwan*
[4]*Department of Mechanical Design Engineering, National Formosa University, Yunlin County 63201, Taiwan*

This paper is concerned with direct energy conversion of waste heat into electrical energy by performing the Olsen cycle on lead nickel niobate zirconate titanate (PNNZT) pyroelectric ceramics undergoing a relaxor-ferroelectric phase transition. First, isothermal bipolar displacement vs. electric field hysteresis loops were measured for different temperatures and electric field spans. The Curie temperature varied between 150 °C and 240 °C as the electric field increased from zero up to 3 MV/m. The energy and power densities of the Olsen cycle on PNNZT were measured by cycling the specimens over a wide range of temperatures, electric fields, and frequencies. A maximum energy density of 1417 J/L/cycle was recorded with 200 μm thick PNNZT cycled at 0.033 Hz between temperatures 20 °C and 240 °C and electric fields 0.3 MV/m and 9.0 MV/m. To the best of our knowledge, this is the largest energy density ever obtained experimentally for any pyroelectric material. In addition, a maximum power density of 78 W/L was measured by cycling the material temperature between 20 °C and 220 °C and applying the electric field between 0.3 MV/m and 9.0 MV/m at 0.09 Hz. *Published by AIP Publishing.* https://doi.org/10.1063/1.5037112

NOMENCLATURE

A	electrode surface area, m^2
b	sample thickness, m
C_p	specific heat of the ferroelectric material, J/kg/°C
D	electric displacement, C/m^2
E	electric field, V/m
E_c	coercive electric field, V/m
E_H	high electric field in Olsen cycle, V/m
E_L	low electric field in Olsen cycle, V/m
f	cycle frequency, Hz
N_D	energy density, J/L
P_D	power density, W/L
P_r	remnant polarization, C/m^2
P_{sat}	saturation polarization, C/m^2
Q	charge, C
T_{cold}	cold temperature reached by the sample, °C
T_{Curie}	Curie temperature, °C
T_{hot}	hot temperature reached by the sample, °C
T_H	hot oil bath temperature, °C
T_L	cold oil bath temperature, °C
T_p	polarization transition temperature, °C

Greek symbols

ε_0	vacuum permittivity (= 8.854×10^{-12} F/m)
ε_r	relative permittivity
$\varepsilon_{r, H}$	relative permittivity at high electric field
$\varepsilon_{r, L}$	relative permittivity at zero electric field
ρ	density of the ferroelectric material, kg/m^3
τ_{ij}	duration of Process i-j, s
τ_{12}	duration of electric field increased from E_L to E_H, s
τ_{23}	duration of temperature increased from T_{cole} to T_{hot}, s
τ_{34}	duration of for electric field decreased from E_H to E_L, s
τ_{41}	duration of temperature decreased from T_{hot} to T_{cold}, s

I. INTRODUCTION

Research and development in waste heat recovery and re-use have received significant attention in recent years. In 2017, around 68% of the energy consumed in the United States was wasted, without having performed any useful function, mainly in the form of low grade heat discharged to the environment.[1] Technologies capable of harvesting such low-temperature thermal energy are attractive for increasing the process efficiencies.[2,3] Organic Rankine cycles use organic working fluids with low boiling points to convert thermal energy at relatively low temperatures into useful mechanical work and electricity.[4] Stirling engines can also convert thermal energy into mechanical energy in a variety of applications such as heat pumps, cryogenic refrigeration, and air liquefaction.[5] Alternatively, thermal energy can be directly converted into electricity thanks to thermoelectric materials and devices taking advantage of the Seebeck effect resulting in electric potential at the junction of two dissimilar metals or semiconductors induced by a temperature difference.[6,7]

a)Author to whom correspondence should be addressed: pilon@seas.ucla.edu. Tel.: +1 310 206 5598. Fax: +1 310 206 4830.

In the last decade, pyroelectric energy harvesting has also received significant attention.[8–10] Pyroelectric materials are capable of converting time-dependent temperature and/or stress directly into electrical energy.[11–28] They can be used to harvest waste heat in industrial applications to increase the process efficiency[13,15] or to convert solar energy used as the hot source while air or water at room temperature can be used as the cold source.[29–31] Pyroelectric materials are a subclass of piezoelectric materials while ferroelectric materials are a subclass of pyroelectric materials. Pyroelectric materials possess a temperature- and stress-dependent spontaneous electric polarization. Linear pyroelectric energy conversion takes advantage of the temperature-dependent spontaneous polarization to passively produce electricity.[32] Unfortunately, such an approach generates only a small amount of electrical energy.[8] By contrast, the Olsen cycle is performed by cycling the temperature and the electric field imposed on the pyroelectric element (PE). The process describes a cycle in the electric displacement vs. electric field diagram of a given pyroelectric material and can greatly enhance the energy and power densities of pyroelectric devices.[8] Various materials have been considered including ceramics (e.g., PZST,[12–15] PLZT,[26,33,34] BaTiO$_3$[9,10]), single crystals (e.g., PMN-PT,[18,35,36] PZN-PT[20,21]), and polymers (e.g., PVDF-TrFE[3,16,22,37–40]). Each material can be operated in different temperature ranges centered around their Curie temperature. Despite progress in material selection, the search for materials with better energy and/or power densities remains essential.[8]

The present study reports experimental measurements of the electrical energy generated by performing the Olsen cycle on commercial Pb(Zr, Ti)O$_3$-Pb(Ni, Nb)O$_3$ (PNNZT) ceramic films. The material performance was assessed under different cycle temperatures, electric fields, and frequencies to determine the optimum conditions that maximize their energy and power densities.

II. BACKGROUND

A. Dielectric hysteresis loops

Figure 1 shows a schematic of isothermal bipolar hysteresis curves of the electric displacement D versus electric field E (D-E loops) exhibited by a pyroelectric/ferroelectric material at two different temperatures T_{cold} and T_{hot} ($>T_{cold}$). These D-E loops travel in a counterclockwise direction. When the temperature of a pyroelectric material exceeds its Curie temperature, the crystallographic structure of the material transitions from ferroelectric to paraelectric and the spontaneous polarization decreases from $P_{sat}(T_{cold})$ to $P_{sat}(T_{hot})$. The coercive field E_c is defined as the minimum electric field required to reach zero displacement, i.e., $D(E_c) = 0$.[41] The remnant polarization P_r corresponds to the electric displacement at zero electric field. The electric displacement D of the material at temperature T under large electric field E can be expressed as[32,42]

$$D(E, T) = \varepsilon_0 \varepsilon_r(E, T)E + P_{sat}(T). \tag{1}$$

The large-field relative permittivity can be estimated by $[\partial D(E,T)/\partial E]_{E_H} = \varepsilon_0 \varepsilon_r(E_H, T)$,[33] where ε_0 is the vacuum permittivity ($= 8.854 \times 10^{-12}$ F/m), $\varepsilon_r(E,T)$ is the material
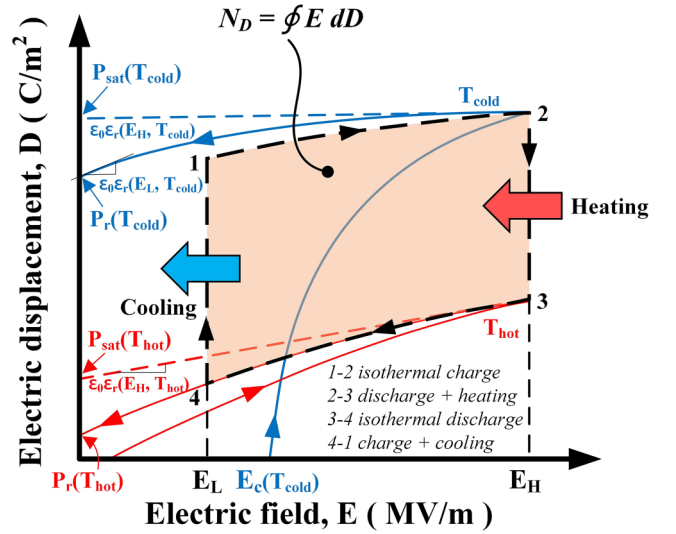

FIG. 1. Electric displacement versus electric field for a typical pyroelectric material at different temperatures. The Olsen power cycle is also shown and represented by the area between 1-2-3-4.

relative permittivity, and E is the applied electric field. The saturation polarization $P_{sat}(T)$ and high field relative permittivity $\varepsilon_r(E_H, T)$ can be estimated from the linear fit of D versus E at high electric field extrapolated to zero electric field. As the electric field E decreases from E_H to zero, the remnant polarization $P_r(T)$ and low field relative permittivity $\varepsilon_r(E_L, T)$ can be observed at 0 MV/m, as illustrated in Fig. 1.

B. Olsen cycle

The Olsen cycle was developed by Olsen and co-workers between 1978 and 1985.[37,39,43–47] It is the electric analog of
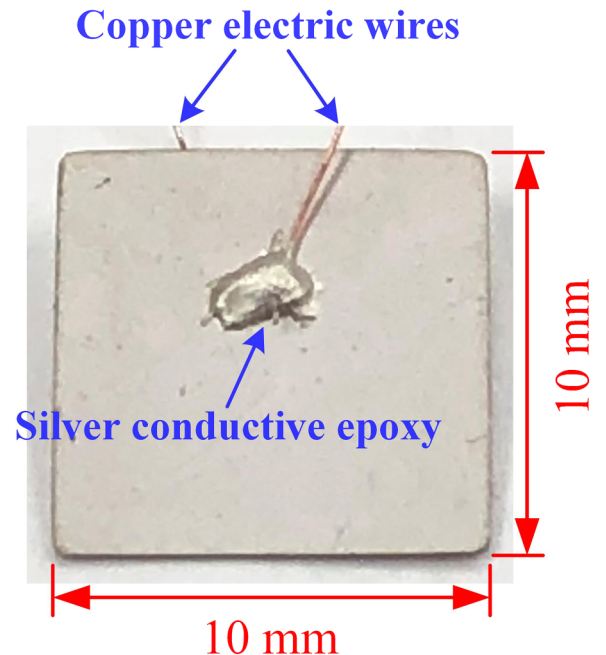

FIG. 2. Photograph of a PNNZT sample used in this study. The electric field was applied across both the silver electrodes of the PNNZT sample though the connected copper electric wires.

the Ericsson cycle in the electric displacement-electric field (*D-E*) diagram of a pyroelectric material, instead of in the pressure-volume diagram of a working fluid. Figure 1 illustrates the Olsen cycle performed on typical ferroelectric material. It consists of two isothermal and two isoelectric field processes. During process 1-2, the pyroelectric element (PE) at temperature T_{cold} is charged by increasing the applied electric field from E_L to E_H. Process 2-3 consists of a discharge caused by increasing the pyroelectric element temperature from T_{cold} to T_{hot} under a constant high electric field E_H. Process 3-4 further discharges the PE by reducing the electric field from E_H to E_L under constant temperature T_{hot}. Finally, process 4-1 closes the cycle by cooling the PE from T_{hot} to T_{cold} under constant electric field E_L.

The area enclosed by the clockwise 1-2-3-4 loop in the *D-E* diagram represents the electric energy converted per unit volume of material per cycle denoted by N_D (in J/L per cycle) and defined as[15]

$$N_D = \oint E\, dD. \qquad (2)$$

The corresponding power density P_D (in W/L) produced by the pyroelectric element is defined as

$$P_D = fN_D, \qquad (3)$$

where f is the cycle frequency defined as $f = 1/(\tau_{12} + \tau_{23} + \tau_{34} + \tau_{41})$, where τ_{ij} is the duration of process *i-j*. For example, τ_{12} and τ_{34} for increasing/decreasing the electric field between $E_L = 0.3$ MV/m and $E_H = 9.0$ MV/m were around 4.2 s while τ_{23} and τ_{41} for heating/cooling between $T_{cold} = 20\,°C$ and $T_{hot} = 220\,°C$ were around 11 s, yielding $f = 0.034$ Hz. Note
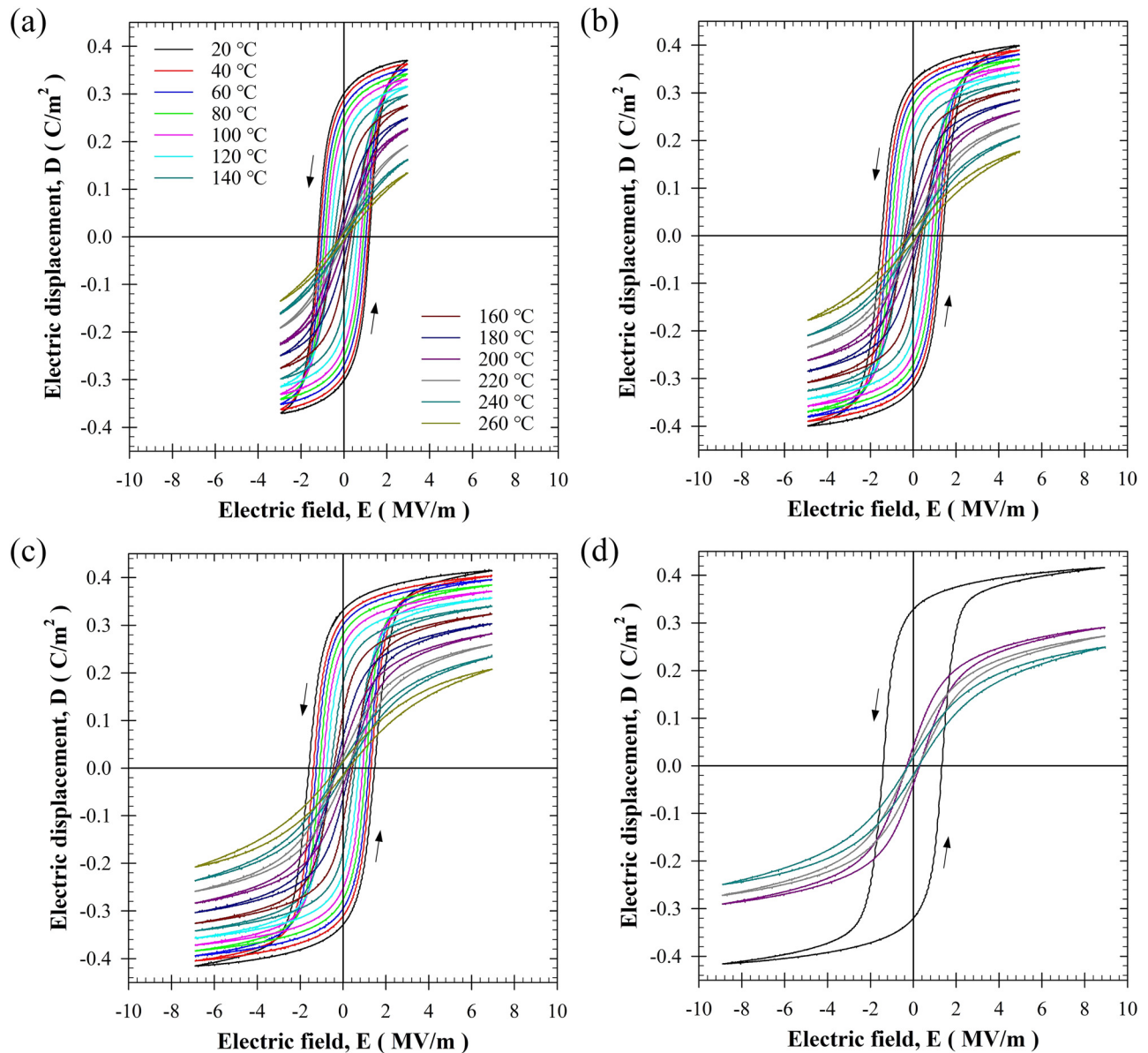

FIG. 3. Bipolar isothermal electric displacement versus electric field (*D–E*) hysteresis curves at various temperatures. The *D-E* loops travel in a counterclockwise direction. The electric field was cycled between (a) −3 and +3 MV/m, (b) −5 and +5 MV/m, (c) −7 and +7 MV/m, and (d) −9 and +9 MV/m at 0.2 Hz and temperature between 20 and 260 °C.

also that the electric field scan rate used in this study was 2.1 MV/m/s. As the material is heated above its Curie temperature T_{Curie}, the isothermal D-E loops gradually become narrow and nearly linear as the material undergoes a phase transition from ferroelectric to paraelectric above T_{Curie}. The electric displacement D also becomes relatively small. Therefore, the energy density N_D enclosed by the cycle 1-2-3-4 (Fig. 1) is larger when phase transition occurs, i.e., when $T_{hot} > T_{Curie}$. Similarly, it can be enlarged by increasing the electric field spans (E_H–E_L). Note, however, that N_D decreases with increasing frequency f as the material may not have time to reach the temperature of the cold and hot sources. Consequently, increasing the power density P_D consists of finding a tradeoff between increasing the cycle frequency f without excessively reducing N_D.

C. Materials

The large piezoelectric constant and electromechanical coupling factor of lead zirconate titanate (PZT) materials make it widely used in sensors, transducers, multilayer capacitors, and haptic/thermal actuators.[48–52] In addition, PZT undergoes a typical ferroelectric to paraelectric phase transition at its Curie temperature, varying from 225 °C to 525 °C depending on its composition.[53] For the purpose of decreasing the sintering temperature and increasing the dielectric properties of PZT, low melting additives and high permittivity materials such as lead nickel niobate [Pb(Ni, Nb)O$_3$] (PNN) can be doped into PZT.[54–57] PNN is a well-known ferroelectric with anomalously large dielectric constant and a broad diffuse phase transition.[58,59] Adding PNN into PZT effectively reduces the PZT Curie temperature while maintaining a high electromechanical coupling factor and a low mechanical quality factor at the morphotrophic phase boundary (MPB).[60–63] Overall, these properties extend the adaptability of PZT in multilayer capacitors, piezoelectric actuators, and energy harvesting devices.[62,63]

The material efficiency η of the Olsen cycle can be expressed as[18,36]

$$\eta = \frac{N_D}{Q_{in}}, \tag{4}$$

where Q_{in} is the energy required to heat and cool the material to the desired temperatures, i.e.,

$$Q_{in} = \oint \rho C_p(T) dT. \tag{5}$$

Here, ρ and C_p are the density and specific heat of the ferroelectric material in kg/m^3 and J/kg/°C, respectively. For example, McKinley *et al.*[28] achieved a material efficiency η of 15.9% with Olsen cycle performed on PMN-28PT.

To date, various structural designs of pyroelectric materials (e.g., micropatterning and microchannels) using micromanufacturing and/or sand blasting techniques have been proposed to enhance heat transfer by convection or radiation in PVDF thin films[64,65] and PZT ceramics[66–72] in order to improve the energy conversion efficiency of materials and devices. Note that reducing the sample thickness should not change the energy per volume N_D achieved under

quasiequilibrium conditions. However, it would have several advantages: (1) it would allow the material to heat and cool more quickly leading to larger power density; (2) it would enable us to achieve the same range of electric fields E_L to E_H with a smaller voltage; (3) it would reduce the risk of breaking sample due to thermal stress or high electric field.[73–76] On the other hand, decreasing the thickness would also reduce the dielectric constant[77] and the robustness of free-standing bulk ferroelectric thin film ceramic and complicate handling.

III. EXPERIMENT

A. Samples

Samples of pyroelectric material PNNZT with dimensions 45 mm × 45 mm × 0.2 mm were purchased from Eleceram Technology Co., Ltd., Taoyuan, Taiwan. Each 45 mm × 45 mm face of samples was coated with a 7 μm thick silver electrode using screen printing technique. The samples had been poled under an electric field of 3.5 MV/m at 120 °C
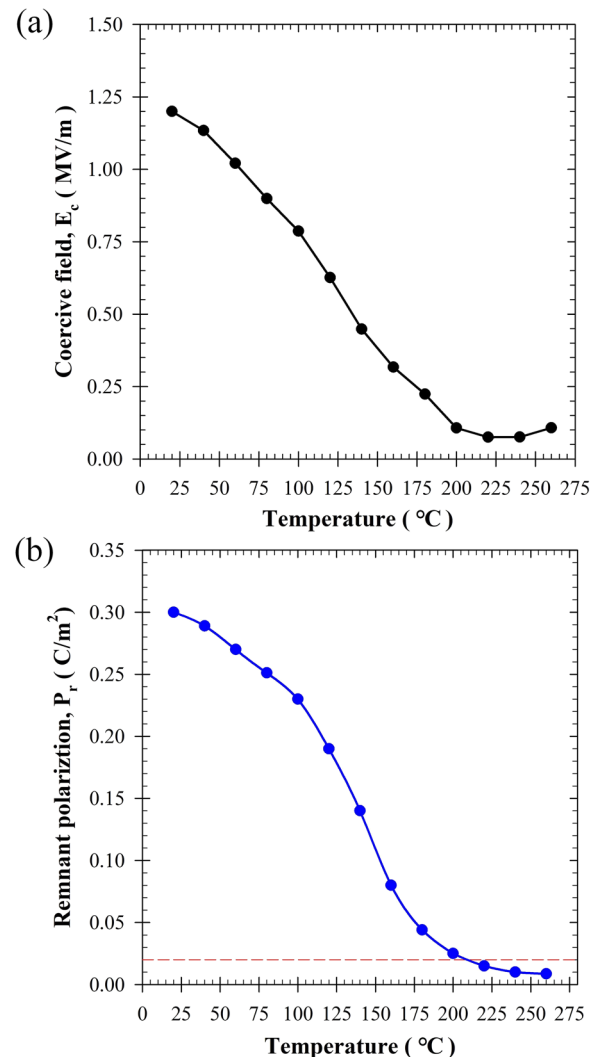

FIG. 4. (a) Coercive field $E_c(T)$ and (b) remnant polarization $P_r(T)$ extracted from isothermal bipolar D-E loops measured with electric field cycled between −3 and +3 MV/m at 0.2 Hz as functions of temperature. The solid lines represent polynomial fits and are plotted to guide the eye.

silicone oil for 20 min. Each specimen was cut into square samples of 10 mm × 10 mm × 0.2 mm by a dicing saw machine. Copper electrical wires were attached to the electrodes with a silver conductivity epoxy. Figure 2 shows a photograph of a representative sample tested in this study.

B. Experimental setup

The electrical subsystem employed in this study consisted of a Sawyer-Tower bridge circuit (impedance = $10^{15}\,\Omega$[78]) identical to that previously used[34,35,38] to measure isothermal *D-E* loops at different temperatures and to monitor and perform the Olsen cycle. The wires bonded to the PNNZT samples were connected to a high voltage power supply imposing the desired electric fields E_L and E_H. They were also connected in series with a capacitor measuring the change in charge Q accumulated at the sample electrodes to determine the electric displacement $D = Q/A$ where A is the PE electrode surface area. In addition, a voltage divider in parallel with the sample and the resistor was used to measure the electric potential V across the sample and the electric field $E = V/b$ where b is the sample thickness.
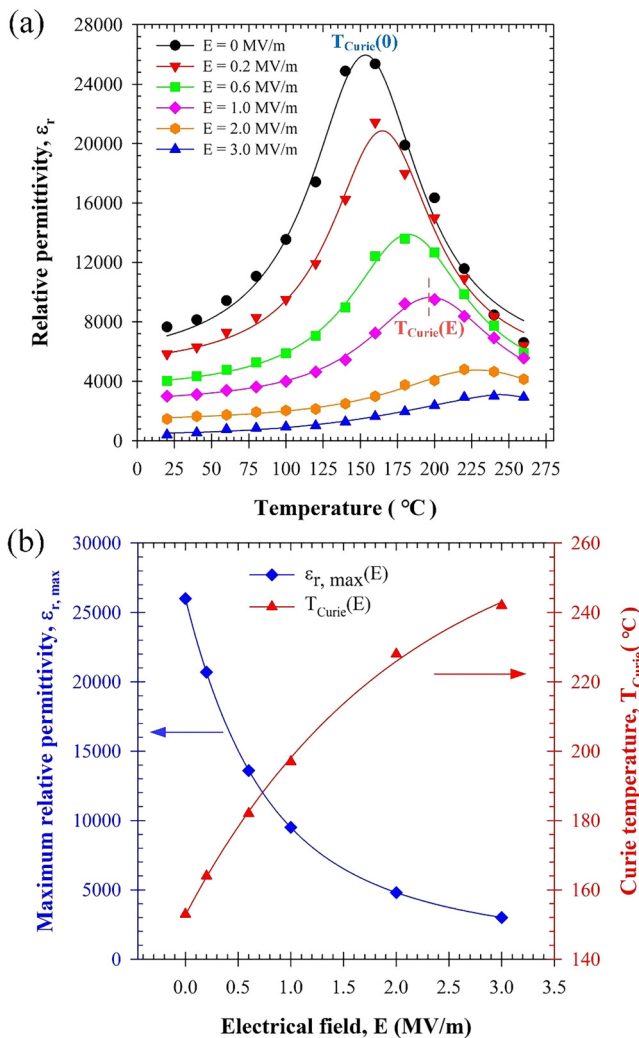
The thermal subsystem consisted of two glass beakers filled with Dow Corning 200 cSt dielectric silicone oil held at constant temperatures T_L and T_H. The hot bath was kept at constant temperature T_H, thanks to a temperature-controlled hot plate, while the cold bath was kept at room temperature T_L. The bath temperatures were monitored with J-type thermocouples. The samples were alternatingly immersed in the two oil baths to create the time-dependent temperature oscillations synchronized with cycling in the electric field E_L and E_H, as required by the Olsen cycle (Fig. 1).

C. Experimental procedure

1. Isothermal D-E Loops

The samples were immersed in a dielectric silicone oil bath long enough to achieve thermal equilibrium conditions before isothermal bipolar *D-E* loops were measured. Loops were measured at various temperatures between 20 °C and 260 °C in 20 °C increments. To do so, the electric field was applied using a triangular voltage signal across the samples
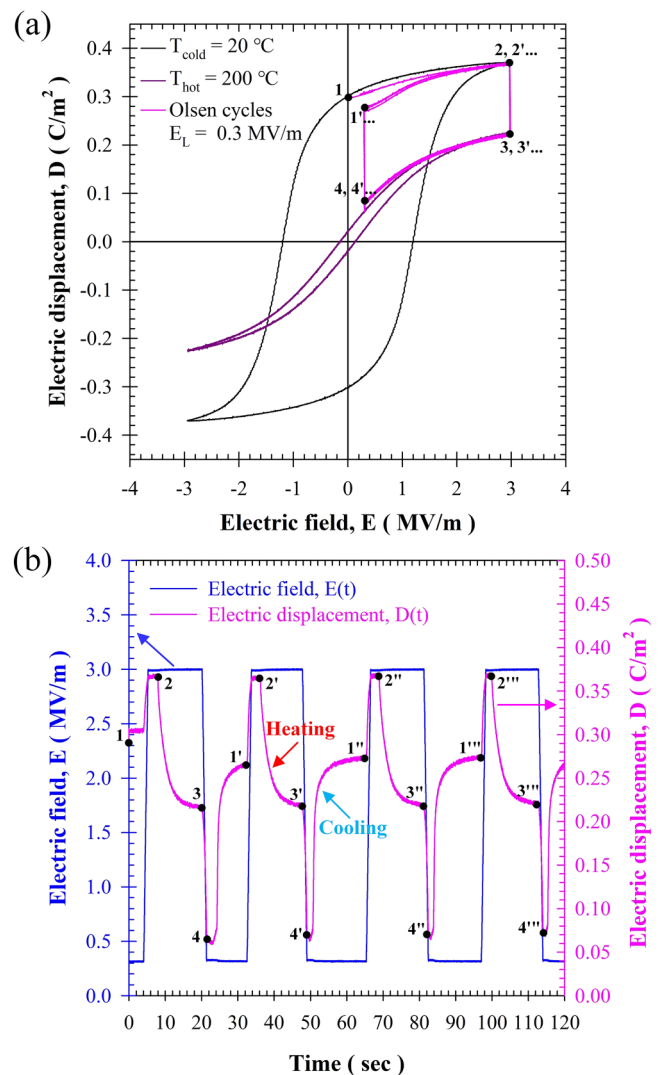

FIG. 5. (a) Relative permittivity $\varepsilon_r(E,T)$ as a function of temperature T and (b) maximum relative permittivity $\varepsilon_{r,max}(E)$ and Curie temperature $T_{Curie}(E)$ as functions of electric field E between 0 MV/m and 3.0 MV/m for PNNZT.

FIG. 6. (a) *D-E* diagram and (b) electric field $E(t)$ and displacement $D(t)$ as functions of time for four consecutive Olsen cycles performed on PNNZT for $E_L = 0.3$ MV/m, $E_H = 3.0$ MV/m, $T_{cold} = 20$ °C, and $T_{hot} = 200$ °C.

at a frequency of 0.2 Hz. This low frequency was chosen to match that at which the Olsen cycle was performed. At such a low frequency, *D-E* loops were not frequency-dependent. *D-E* loops were collected under different high electric field E_H ranging between 3.0 MV/m and 9.0 MV/m in 2.0 MV/m increment.

2. Olsen cycle

In this study, the Olsen cycle was performed on PNNZT specimens with various electric fields E_L and E_H, oil bath temperatures T_L and T_H, and operating frequency *f*. The low electric field E_L varied between 0.0 and 0.6 MV/m, the high electric field E_H between 3.0 and 9.0 MV/m, and the operating frequency *f* between 0.03 Hz and 0.12 Hz. The cold oil bath temperature T_L was maintained at 20 °C while the hot oil bath temperature T_H varied from 180 °C to 260 °C. The resulting energy N_D and power P_D densities were

systematically estimated using Eqs. (2) and (3) in order to identify the optimum operating conditions. The trapezoidal rule was utilized to estimate the integral of Eq. (2).

IV. RESULT AND DISCUSSION

A. Material characterization

1. Isothermal bipolar D-E loops

Figure 3 shows the isothermal bipolar *D-E* loops measured at temperatures ranging from 20 °C to 260 °C for electric field oscillating between (a) −3 and +3 MV/m, (b) −5 and +5 MV/m, (c) −7 and +7 MV/m, and (d) −9 and +9 MV/m. It indicates that (i) the electric displacement decreased with increasing temperature and (ii) the *D-E* loops degenerated into narrow and quasilinear loops as the material underwent phase transition from ferroelectric to paraelectric. The *D-E* loops for temperatures below ∼220 °C correspond
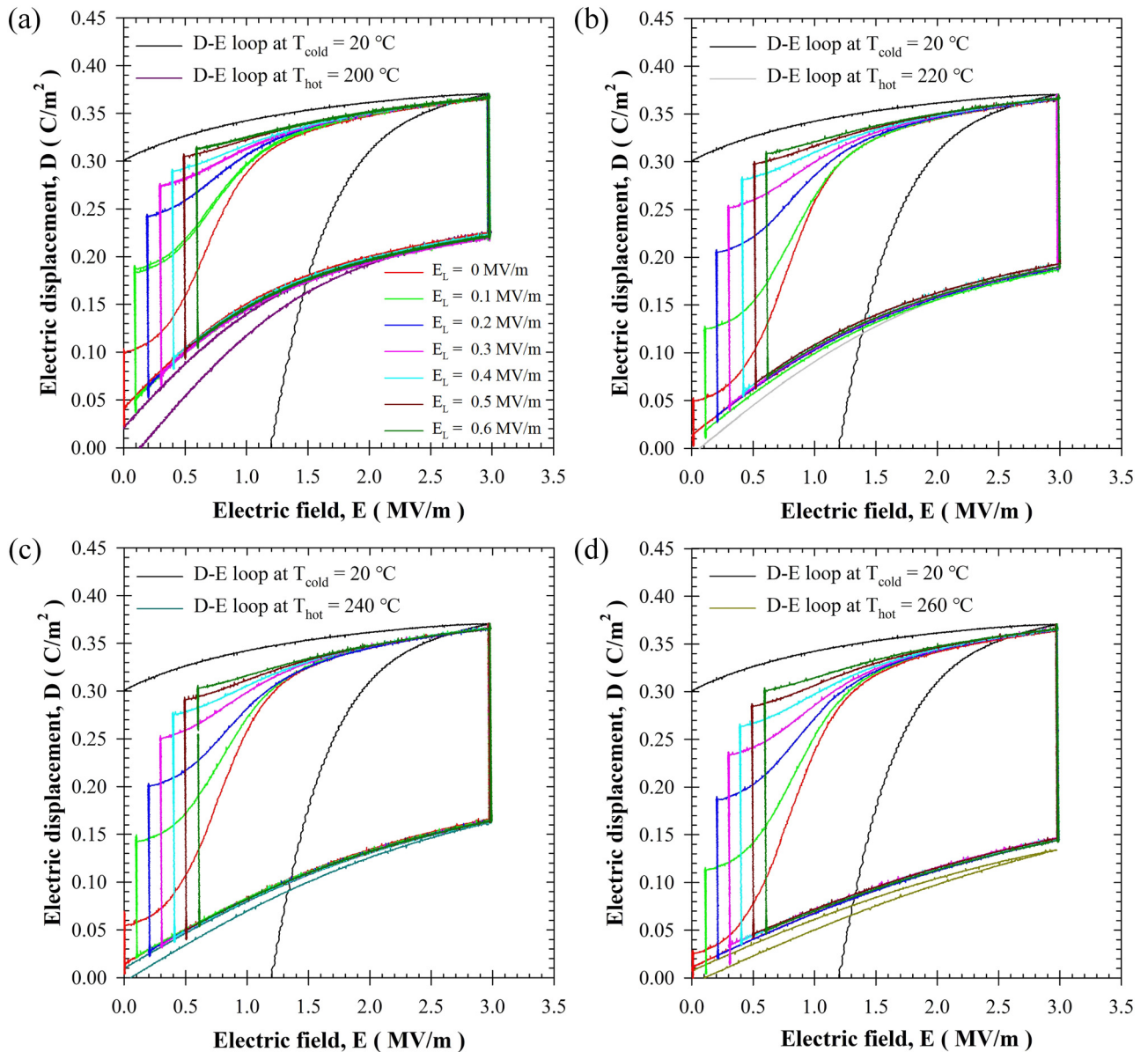

FIG. 7. Experimental Olsen cycles performed on PNNZT plotted in the D-E diagram for $E_H = 3.0$ MV/m and E_L varying from 0 MV/m to 3.0 MV/m and for temperature $T_{cold} = 20$ °C and (a) $T_{hot} = 200$ °C, (b) $T_{hot} = 220$ °C, (c) $T_{hot} = 240$ °C, and (d) $T_{hot} = 260$ °C at low frequency *f* around 0.04 Hz.

to the ferroelectric phase while those at 240 °C and 260 °C indicate that the material was in the ergodic relaxor phase.

Figure 4 shows the coercive field E_c and the remnant polarization P_r as functions of temperature for the PNNZT samples considered. At 20 °C, the D-E loop had large coercive field E_c around 1.2 MV/m and large remnant polarization P_r of 0.3 C/m² indicative of high coercive strength typical of hard ferromagnetic materials.[41,79] The remnant polarization gradually decreased and dropped below the transition polarization of ~0.02 C/m² observed at polarization transition temperature T_p around 220-225 °C. Here, the polarization transition temperature T_p was defined as the temperature corresponding to a negligibly small remnant polarization ($P_r < 0.02$ C m⁻²). Similarly, E_c reached its minimum near 0 MV/m at 220-225 °C.

2. Curie temperature

For a given electric field E, the temperature corresponding to the maximum dielectric constant is usually defined as the Curie temperature $T_{Curie}(E)$.[79] Figure 5(a) plots the relative permittivity as a function of temperature for electric field varying between the small field (0 MV/m) and the high field (3.0 MV/m) for PNNZT at 0.2 Hz as functions of temperature. It also shows the associated fit based on Lorentzian or Cauchy-Lorentz distribution function ($R^2 > 0.95$). The relative permittivity was estimated from the partial derivative $(\partial D/\partial E)_T$ for the portion of isothermal bipolar D-E loops near 0 MV/m and E_H. Figure 5(b) shows the maximum relative permittivity $\varepsilon_{r,max}$ and Curie temperature T_{Curie} as functions of imposed electric field E corresponding to $(\partial \varepsilon_r/\partial T)_E = 0$ estimated from the Lorentzian fit of $\varepsilon_r(T)$. It indicates that the Curie temperature at zero field $T_{Curie}(E=0)$ was around 150 °C falling below the polarization transition temperature of 220 °C and increased to $T_{Curie}(E_H)$ around 240 °C under high electric field $E_H = 3.0$ MV/m. This can be attributed to the fact that large electric fields induce a ferroelectric state at temperatures above the zero-field Curie temperature. Indeed, the large electric field forcibly converts relaxor polar nanoregions into ferroelectric micron-sized domains responsible for an increase in T_{Curie} with increasing electric field.[80] Based on the Curie temperature, we speculate that the mole fraction of PNN in the PNNZT samples investigated was around 50 mol. %.[81]

B. Olsen cycle

The Olsen cycle was performed on the PNNZT samples between different electric fields and temperatures, and at different frequencies. Note that at low frequencies ($f < 0.04$ Hz), the minimum and maximum sample temperatures reached the cold and hot bath temperatures, i.e., $T_{cold} = T_L$ and $T_{hot} = T_H$. To make sure the results were repeatable for each testing condition, the Olsen cycles were performed at least 3-4 times before changing the operating conditions (e.g., the high electric E_H). Figure 6(a) presents, in the D-E diagram, four consecutive Olsen cycles performed experimentally on PNNZT with $T_{cold} = 20$ °C, $T_{hot} = 200$ °C, $E_L = 0.3$ MV/m, and $E_H = 3.0$ MV/m at 0.033 Hz. It is interesting to note that the successive Olsen cycles overlap and closely followed the isothermal bipolar D-E loops at 20 °C and 200 °C at 0.033 Hz.

It also clearly illustrates that the samples were repolarized with increasing E during process 1′-2′ of the subsequent Olsen cycle. Figure 6(b) presents the electric field E and electric displacement D as functions of time corresponding to the Olsen cycles plotted in Fig. 6(a). During each process, 2-3 and 4-1 thermal equilibrium was reached and the temporal evolution of the electric field and displacement of the PNNZT sample were repeatable from one cycle to the next.

3. Effect of low electric field E_L and high sample temperature T_{hot}

Figure 7 shows various Olsen cycles in the D-E diagram performed on PNNZT with low electric field E_L ranging from 0 MV/m to 0.6 MV/m and high sample temperature T_{hot} equals to (a) 200 °C, (b) 220 °C, (c) 240 °C, and (d) 260 °C. The high electric field, low sample temperature, and
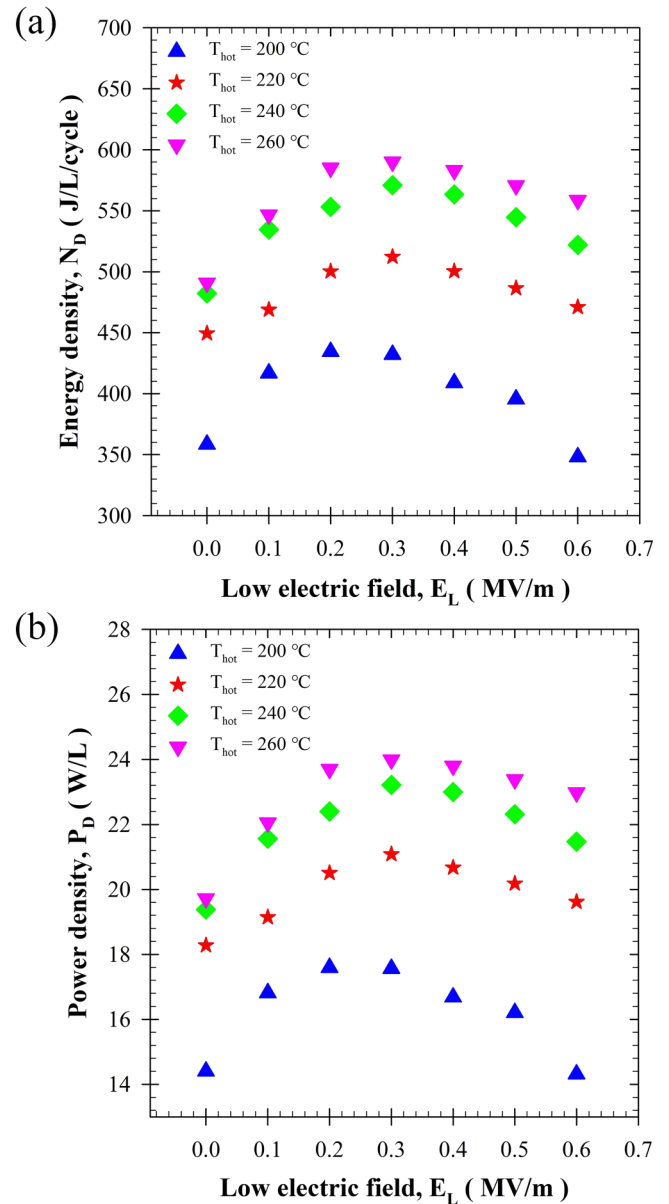

FIG. 8. (a) Energy N_D and (b) power P_D densities generated by PNNZT as functions of E_L for high temperatures T_{hot} between 200 °C and 260 °C corresponding to the Olsen cycles plotted in Fig. 7.
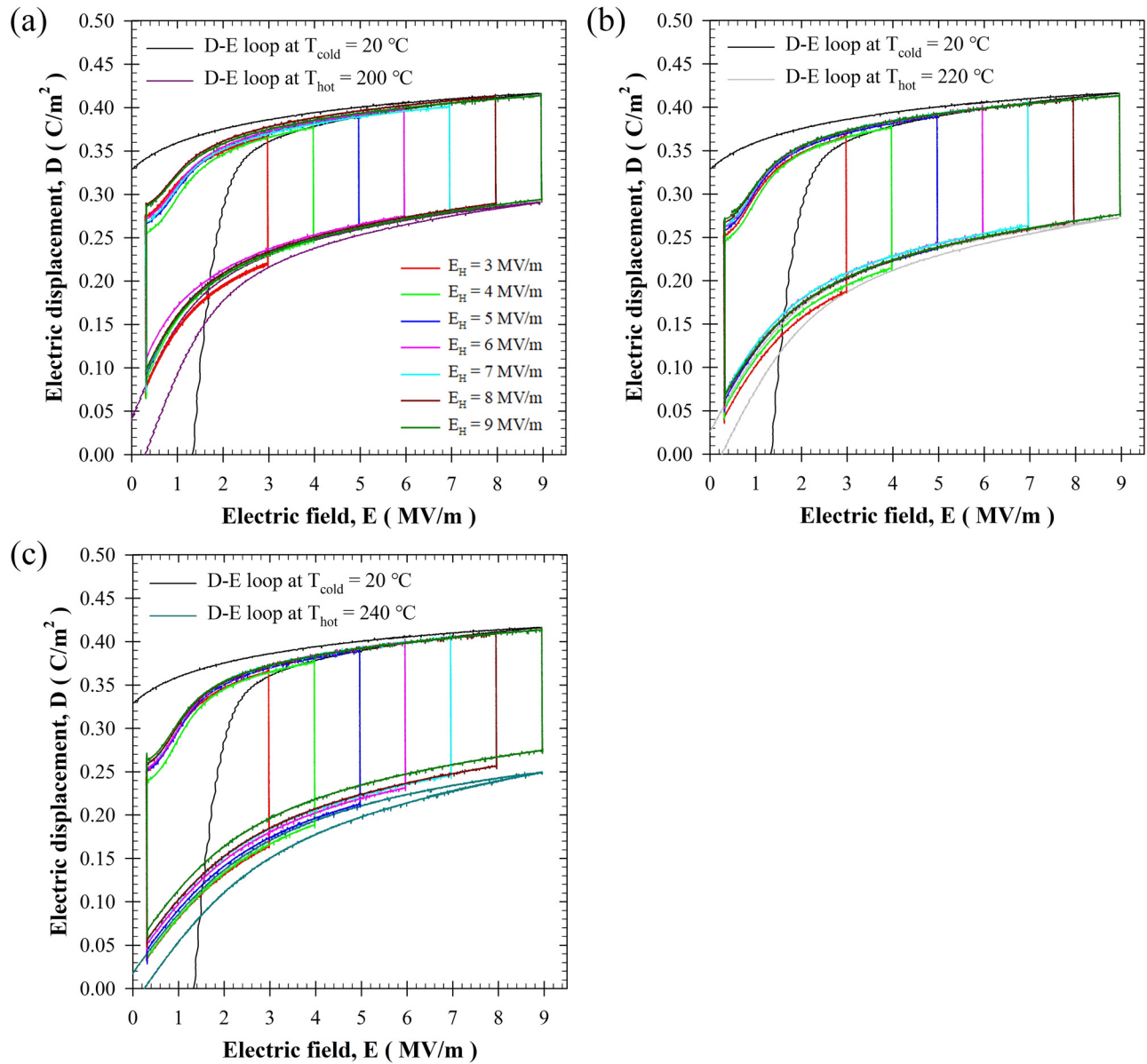
FIG. 9. Experimental Olsen cycle performed on PNNZT plotted in the *D-E* diagram for $E_L = 0.3$ MV/m and E_H varying from 3.0 MV/m to 9.0 MV/m and for temperature $T_{cold} = 20\,°C$ and (a) $T_{hot} = 200\,°C$, (b) $T_{hot} = 220\,°C$, or (c) $T_{hot} = 240\,°C$ at low frequency f around 0.04 Hz.

frequency were set at $E_H = 3.0$ MV/m, $T_{cold} = 20\,°C$, and $f \approx$ 0.04 Hz, respectively. Figure 7 indicates that during process 4-1 of the Olsen cycle, the amplitude changes in the electric displacement (D_1-D_4) decreased with decreasing E_L. In fact, the subsequent process 1-2 in the Olsen cycle did not follow the isothermal bipolar *D-E* loops at any given temperature T_{hot}. This was due to the fact that the PNNZT sample lost its polarization and was not able to fully repolarize during process 4-1 performed under low electric field. For $E_L \leq 0.2$ MV/m, the sample recovered its polarization during process 1-2 as the electric field increased. Furthermore, ideally, the electrical impedance of the PNNZT samples is infinite. In practice, however, the impedance decreased with increasing temperature.[82] This is evident in Fig. 7(d) when the PNNZT was heated to 260 °C under $E_H = 3.0$ MV/m (process 2-3). The electric displacement did not follow the *D-E* isothermal loop at T_{hot} indicating the presence of leakage current

through the sample. In addition, the sample loses most of polarization when T_{hot} exceeds T_{Curie}, and the dipoles are harder to realign at low electrical field E_L during the cooling process due to the slow dipole relaxation inherent to ferroelectric-relaxor materials.[33,83]

Figure 8 shows (a) the energy N_D and (b) power P_D densities generated by PNNZT as functions of E_L for $E_H = 3.0$ MV/m and, T_{hot} varying from 200 °C to 260 °C, corresponding to the cycles shown in Fig. 7. Figure 8 indicates that the maximum energy and power densities were obtained for $E_L = 0.3$ MV/m and $T_{hot} = 260\,°C$. This can be attributed to the fact that, at 260 °C, the *D-E* loop of PNNZT was slim and quasilinear due to phase transformation to paraelectric. For $T_{hot} = 200\,°C$, the energy density reduced from 590 to 491 J/L/cycle as E_L decreased from 0.3 to 0 MV/m due to the loss of polarization upon cooling during process 4-1, as previously discussed. Furthermore, increasing the low electric
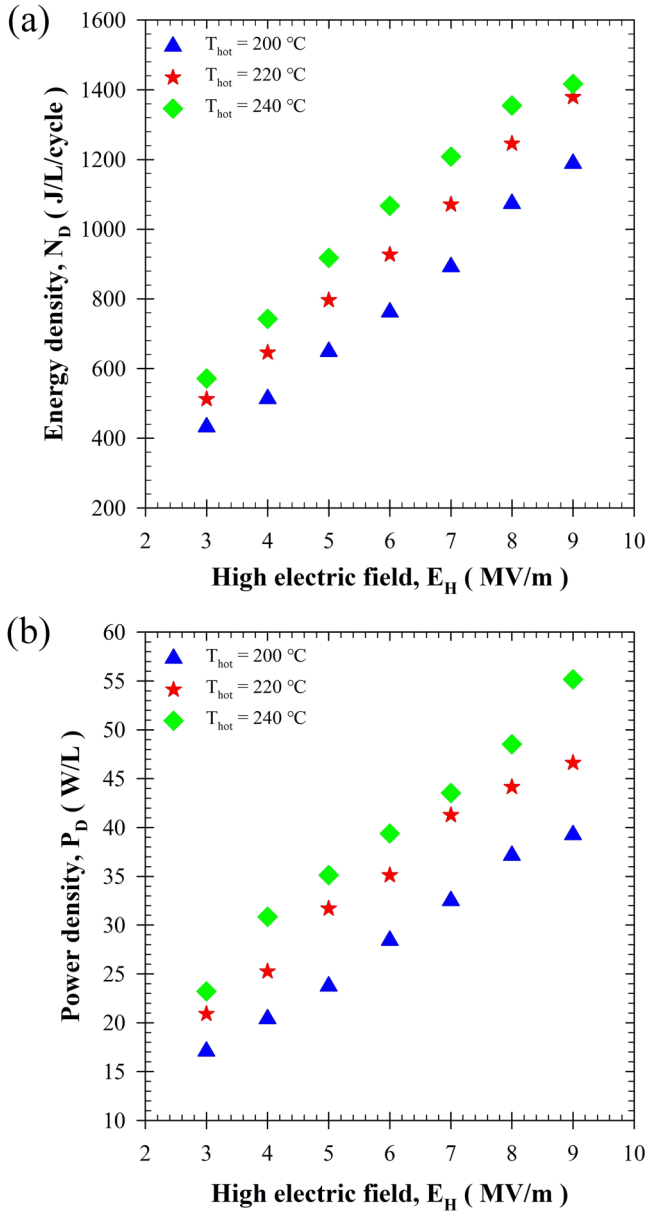
FIG. 10. (a) Energy N_D and (b) power P_D densities generated by PNNZT as functions of E_H for high temperatures T_{hot} between 200 °C and 240 °C corresponding to the Olsen cycles plotted in Fig. 9.

field E_L from 0.3 to 0.6 MV/m reduced the energy density from 590 to 559 J/L/cycle due to the smaller electric field span (E_H-E_L). Therefore, the optimum low electric field E_L corresponded to a tradeoff between increasing the electric field span (E_H-E_L) and ensuring that the sample quickly recovered its polarization upon cooling during process 4-1. Similarly, Fig. 8(b) indicates that the largest power density of 24 W/L was found for $f \approx 0.04$ Hz with $E_L = 0.3$ MV/m and $T_{hot} = 260$ °C. Finally, when T_{hot} was below 220 °C, the maximum energy and power densities were reached for $E_L = 0.2$ MV/m.

4. Effect of high electric field E_H and high sample temperature T_{hot}

Figure 9 shows the different Olsen cycles performed on PNNZT in the D-E diagram with E_H ranging from 3.0 MV/m

to 9.0 MV/m and T_{hot} equals to (a) 200 °C, (b) 220 °C, and (c) 240 °C for $f \approx 0.04$ Hz with E_L and T_{cold} fixed at 0.3 MV/m and 20 °C, respectively. It indicates that increasing the electric field span (E_H-E_L) led to larger energy density. Note that, here, the Olsen cycle loops overlapped with the isothermal bipolar D-E loops at the corresponding temperatures.

Figure 10 shows (a) the energy N_D and (b) power P_D densities measured as functions of high electric field E_H corresponding to the Olsen cycles reported in Fig. 9. It is evident that both the energy and power densities increased almost linearly with increasing high electric field E_H for a given high temperature T_{hot}. They also increased with increasing T_{hot} for a given E_H. For example, the energy density increased from 432 to 1188 J/L/cycle as E_H increased from 3.0 MV/m to 9.0 MV/m at $T_{hot} = 200$ °C. In addition, the maximum energy density achieved was 1417 J/L/cycle for $E_H = 9$ MV/m and $T_{hot} = 240$ °C. To the best of our knowledge, this is the largest energy density achieved experimentally using the Olsen cycle for all pyroelectric materials reported to date exceeding the 1060 J/L/cycle recently obtained with 150 nm thick PMN-PT thin film.[84] Furthermore, other large energy density N_D reported in the literature include (i) 900 J/L/cycle for 60/40 P(VDF-TrFE)[16] and (ii) 1013 J/L/cycle for 7/65/35 PLZT.[33] This maximum energy density achieved was limited by the dielectric strength of the sample reported to be in the range 10-25 MW/m.[85,86] Finally, operation under high electric field and/or temperature in excess of $E_H = 9.0$ MV/m and $T_{hot} = 240$ °C significantly stressed the PNNZT samples and resulted in leakage current and microcrack formation within the sample.[87,88]

5. Effect of cycle frequency f and high electric field E_H

Figure 11 plots both the energy N_D and power P_D densities achieved by PNNZT samples as functions of cycle frequency for $E_H = 7.0$ MV/m and 9.0 MV/m and oil bath temperature T_H equals to (a, b) 180 °C, (c, d) 200 °C, and (e, f) 220 °C. In all cases, the low electric field and cold oil bath temperature were $E_L = 0.3$ MV/m and $T_L = 20$ °C, respectively. Figure 11 indicates that, as the electric field and temperature increased, the energy density N_D reached a maximum of 1379 J/L/cycle at the lowest frequency of 0.034 Hz and decreased almost linearly with increasing cycle frequency. This can be attributed to the fact that, during processes 2-3 (heating) and 4-1 (cooling), the dipole could not be fully realigned with increasing frequency due to the slow dipole relaxation inherent to ferroelectric-relaxor materials particularly since T_H was below $T_{Curie}(E_H)$.[33,72] In addition, Figs. 11(a)–11(e) indicate that the power density P_D reached its maximum around 0.1 Hz for all conditions tested. These results illustrate the tradeoff previously mentioned between increasing frequency without excessively decreasing $N_D(f)$ in order to maximize the power density.

Table I summarizes the operating conditions corresponding to the maximum energy density $N_{D,max}$, and power density $P_{D,max}$ for T_{hot} equals 180 °C, 200 °C, 220 °C, and 240 °C. It indicates that maximum energy density $N_{D,max}$ increased from 911 J/L/cycle to 1417 J/L/cycle as T_H
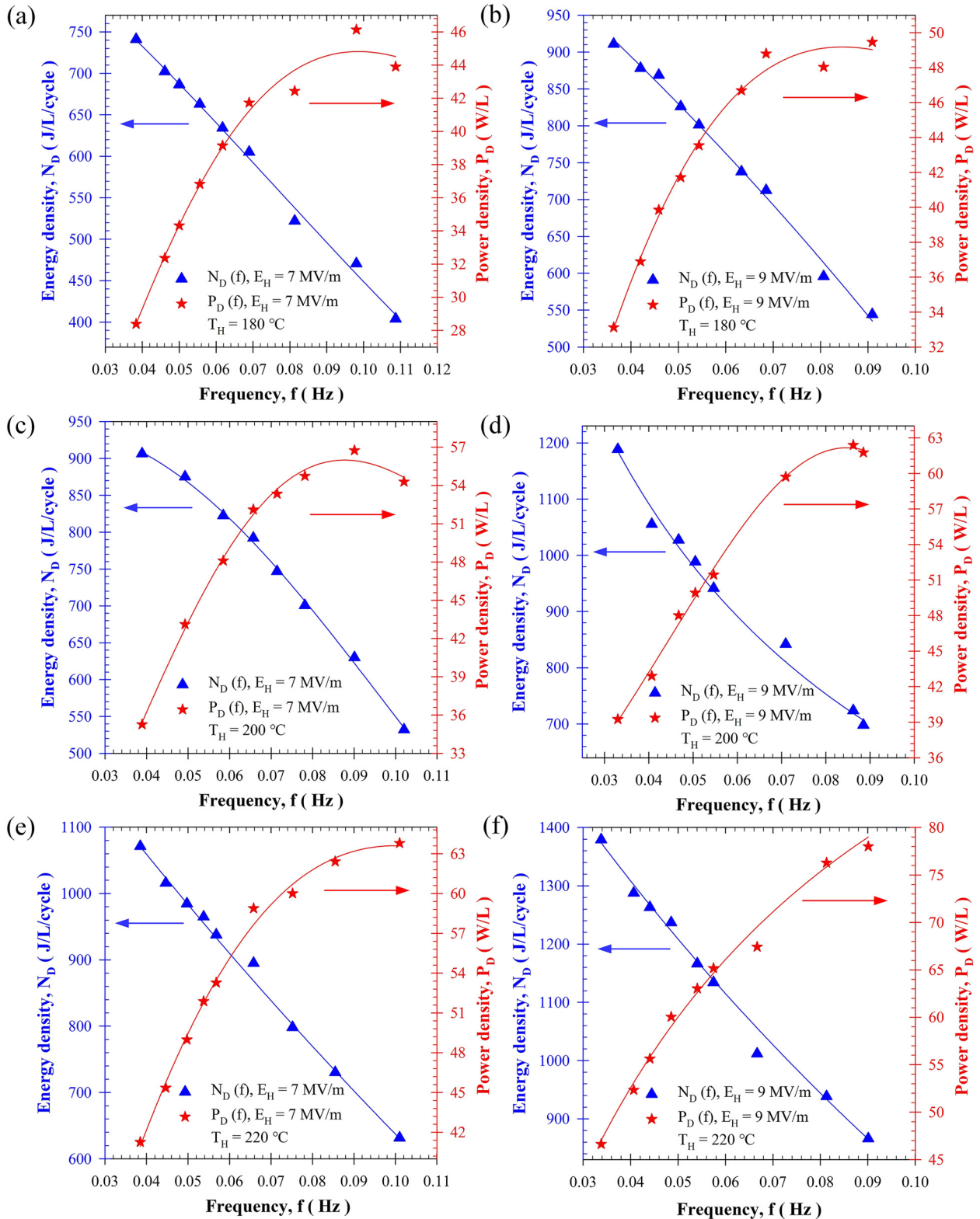
FIG. 11. Energy and power densities obtained with PNNZT as a function of cycle frequency for $E_L = 0.3$ MV/m, $T_L = 20$ °C with (a) $E_H = 7.0$ MV and $T_H = 180$ °C; (b) $E_H = 9.0$ MV and $T_H = 180$ °C; (c) $E_H = 7.0$ MV and $T_H = 200$ °C; (d) $E_H = 9.0$ MV and $T_H = 200$ °C; (e) $E_H = 7.0$ MV and $T_H = 220$ °C; (f) $E_H = 9.0$ MV and $T_H = 220$ °C.

increased from 180 °C to 240 °C. In all cases, the optimum electric fields were $E_L = 0.3$ MV/m and $E_H = 9.0$ MV/m while the operating frequency was small around 0.03-0.04 Hz. Table I also shows that the maximum power density $P_{D,max}$

was 78 W/L for a cycle frequency of 0.09 Hz and a corresponding N_D of 866 J/L/cycle. For comparison, linear pyro-electric energy conversion using PZT-5H can achieve energy N_D and power P_D densities typically around 0.9 J/L/cycle and

TABLE I. Maximum energy and power densities achieved using the Olsen cycle for PNNZT, temperature ranges, operating electric fields, and cycle frequencies.

T_L (°C)	T_H (°C)	E_L (MV/m)	E_H (MV/m)	f (Hz)	$N_{D,max}$ (J/L/cycle)
20	180	0.3	9.0	0.036	911
20	200	0.3	9.0	0.033	1188
20	220	0.3	9.0	0.034	1379
20	240	0.3	9.0	0.039	1417

T_L (°C)	T_H (°C)	E_L (MV/m)	E_H (MV/m)	f (Hz)	$P_{D,max}$ (W/L)
20	180	0.3	9.0	0.091	49
20	200	0.3	9.0	0.086	62
20	220	0.3	9.0	0.090	78

0.4 W/L, respectively, and cycled temperature between 50 and 110 °C.[89]

V. CONCLUSION

This study presented experimental measurements of energy and power densities generated by the Olsen cycle performed on PZT doped with lead nickel niobate [Pb(Ni, Nb)O$_3$] (PNN). First, the polarization transition temperature T_p and Curie temperature T_{Curie} under zero-field of the PNNZT samples were found to be 220 °C and 150 °C, respectively. In addition, Curie temperature T_{Curie} under large field (3.0 MV/m) was 240 °C due to relaxor polar nanoregions being forcibly converted into ferroelectric micron-sized domains by the large electric field. Performing the Olsen cycle such that the material underwent an ergodic relaxor-ferroelectric phase transition enhanced the energy and power densities of PNNZT. A maximum energy density of 1417 J/L/cycle was generated by PNNZT under thermal quasiequilibrium conditions (i.e., low frequency) by cycling the temperature between 20 and 240 °C and the electric field between 0.3 and 9.0 MV/m. To the best of our knowledge, this is the largest energy density produced by any pyroelectric material to date. Finally, a maximum power density of 78 W/L was recorded at 0.09 Hz operating between 20 °C and 220 °C.

SUPPLEMENTARY MATERIAL

The data for the experimental D-E loops shown in Fig. 7 are available in digital format in the supplementary material.

ACKNOWLEDGMENTS

[1]Lawrence Livermore National Laboratory 2018, 2017 U.S. Energy Flow Trends, see https://flowcharts.llnl.gov/.

[2]Y. Ammar, S. Joyce, R. Norman, Y. Wang, and A. P. Roskilly, "Low grade thermal energy sources and uses from the process industry in the UK," Appl. Energy **89**, 3–20 (2012).

[3]S. Hunter, N. Lavrik, T. Bannuru, S. Mostafa, S. Rajic, and P. Datskos, "Development of MEMS based pyroelectric thermal energy harvesters," Proc. SPIE **8035**, 80350V (2011).

[4]A. Desideri, S. Gusev, M. Van den Broek, V. Lemort, and S. Quoilin, "Experimental comparison of organic fluids for low temperature ORC (organic Rankine cycle) systems for waste heat recovery applications," Energy **97**, 460–469 (2016).

[5]D. G. Thombare and S. K. Verma, "Technological development in the Stirling cycle engines," Renew. Sustain. Energy Rev. **12**, 1–38 (2008).

[6]E. A. Skrabek and J. W. McGrew, "Pioneer 10 and 11 RTG performance update," Space Nucl. Power Syst. **7**, 201–204 (1987).

[7]S. B. Riffat and X. Ma, "Thermoelectrics: A review of present and potential applications," Appl. Therm. Eng. **23**, 913–935 (2003).

[8]L. Pilon and I. McKinley, "Pyroelectric energy conversion," Annu. Rev. Heat Transf. **19**, 279–334 (2016).

[9]B. Bhatia, A. R. Damodaran, H. Cho, L. W. Martin, and W. P. King, "High-frequency thermal-electrical cycles for pyroelectric energy conversion," J. Appl. Phys. **116**, 194509 (2014).

[10]B. Bhatia, H. Cho, J. Karthik, J. Choi, D. G. Cahill, L. W. Martin, and W. P. King, "High power density pyroelectric energy conversion in nanometer-thick BaTiO$_3$ films," Nanosc. Microsc. Therm. Eng. **20**, 137–146 (2016).

[11]R. B. Olsen, "Ferroelectric conversion of heat to electrical energy – A demonstration," J. Energy **6**, 91–95 (1982).

[12]R. B. Olsen and D. D. Brown, "High-efficiency direct conversion of heat to electrical energy related pyroelectric measurements," Ferroelectrics **40**, 17–27 (1982).

[13]R. B. Olsen, D. A. Bruno, and J. M. Briscoe, "Cascaded pyroelectric energy converter," Ferroelectrics **59**, 205–219 (1984).

[14]R. B. Olsen, D. A. Bruno, and J. M. Briscoe, "Pyroelectric conversion cycles," J. Appl. Phys. **58**, 4709–4716 (1985).

[15]R. B. Olsen, D. A. Bruno, J. M. Briscoe, and W. F. Butler, "A pyroelectric energy converter which employs regeneration," Ferroelectrics **38**, 1–4 (1981).

[16]R. B. Olsen and D. A. Bruno, "Pyroelectric conversion materials", in *Proceedings of the 21st Intersociety Energy Conversion Engineering Conference*, 25–29 August 1986 (American Chemical Society, San Diego, CA), pp. 89–93.

[17]L. Kouchachvili and M. Ikura, "High performance pyroelectric converter", in *Proceedings of the 6th IASTED International Conference on European Power and Energy Systems, Rhodes, Greece,* 26–28 June 2006 (Acta Press, 2006), pp. 366–371.

[18]G. Sebald, S. Pruvost, and D. Guyomar, "Energy harvesting based on Ericsson pyroelectric cycles in a relaxor ferroelectric ceramic," Smart Mater. Struct. **17**, 1–6 (2008).

[19]D. Guyomar, S. Pruvost, and G. Sebald, "Energy harvesting based on FE–FE transition in ferroelectric single crystals," IEEE Trans. Ultrason. Ferroelectr. Freq. Control **55**, 279–285 (2008).

[20]A. Khodayari, S. Pruvost, G. Sebald, D. Guyomar, and S. Mohammadi, "Nonlinear pyroelectric energy harvesting from relaxor single crystals," IEEE Trans. Ultrason. Ferroelectr. Freq. Control **56**, 693–699 (2009).

[21]I. M. McKinley, R. Kandilian, and L. Pilon, "Waste heat energy harvesting using the Olsen cycle on 0.945 Pb(Zn$_{1/3}$Nb$_{2/3}$)O$_3$–0.055 PbTiO$_3$ single crystals," Smart Mater. Struct. **21**, 035015 (2012).

[22]H. Nguyen, A. Navid, and L. Pilon, "Pyroelectric energy converter using co-polymer P (VDF-TrFE) and Olsen cycle for waste heat energy harvesting," Appl. Therm. Eng. **30**, 2127–2137 (2010).

[23]F. Y. Lee, A. Navid, and L. Pilon, "Pyroelectric waste heat energy harvesting using heat conduction," Appl. Therm. Eng. **37**, 30–37 (2012).

[24]I. M. McKinley and L. Pilon, "Phase transitions and thermal expansion in pyroelectric energy conversion," Appl. Phys. Lett. **102**, 023906 (2013).

[25]A. Navid, C. S. Lynch, and L. Pilon, "Purified and porous poly (vinylidene fluoride-trifluoroethylene) thin films for pyroelectric infrared sensing and energy harvesting," Smart Mater. Struct. **19**, 055006 (2010).

[26]T. Chin, F. Y. Lee, I. M. McKinley, S. Goljahi, C. S. Lynch, and L. Pilon, "Pyroelectric waste heat energy harvesting using 9.5/65/35 PLZT ceramics," IEEE Trans. Ultrason. Ferroelectr. Freq. Control **59**, 2373 (2012).

[27]I. M. McKinley, S. Goljahi, C. S. Lynch, and L. Pilon, "A novel thermally biased mechanical energy conversion cycle," J. Appl. Phys. **114**, 224111 (2013).

[28]I. M. McKinley, F. Y. Lee, and L. Pilon, "A novel thermomechanical energy conversion cycle," Appl. Energy **126**, 78–89 (2014).

[29]Q. Zhang, A. Agbossou, Z. Feng, and M. Cosnier, "Solar micro-energy harvesting with pyroelectric effect and wind flow," Sens. Actuators A Phys. **168**, 335–342 (2011).

[30]M. Sharma, A. Chauhan, R. Vaish, and V. S. Chauhan, "Finite element analysis on solar energy harvesting using ferroelectric polymer," Solar Energy **115**, 722–732 (2015).

[31]M. Sharma, A. Chauhan, R. Vaish, and V. S. Chauhan, "Pyroelectric materials for solar energy harvesting: A comparative study," Smart Mater. Struct. **24**, 105013 (2015).

[32]S. B. Lang and D. K. Das-Gupta, *Handbook of Advanced Electronic and Photonic Materials and Devices* (Academic Press, San Diego, CA, 2001), Vol. 4.

[33]F. Y. Lee, H. R. Jo, C. S. Lynch, and L. Pilon, "Pyroelectric energy conversion using PLZT ceramics and the ferroelectric–ergodic relaxor phase transition," Smart Mater. Struct. **22**, 025038 (2013).

[34]F. Y. Lee, S. Goljahi, I. McKinley, C. S. Lynch, and L. Pilon, "Pyroelectric waste heat energy harvesting using relaxor ferroelectric 8/65/35/ PLZT and the Olsen cycle," Smart Mater. Struct. **21**, 025021 (2012).

[35]R. Kandilian, A. Navid, and L. Pilon, "The pyroelectric energy harvesting capabilities of PMN-PT near the morphotropic phase boundary," Smart Mater. Struct. **20**, 055020 (2011).

[36]J. Fang, H. Frederich, and L. Pilon, "Harvesting nanoscale thermal radiation using pyroelectric materials," Int. J. Heat Tran. **132**, 092701 (2010).

[37]M. Ikura, "Conversion of low-grade heat to electricity using pyroelectric copolymer," Ferroelectrics **267**, 403–408 (2002).

[38]A. Navid and L. Pilon, "Pyroelectric energy harvesting using Olsen cycles in purified and porous poly(vinylidene fluoride-trifluoroethylene) thin films," Smart Mater. Struct. **20**, 025012 (2011).

[39]R. B. Olsen, D. A. Bruno, and J. M. Briscoe, "Pyroelectric conversion cycle of vinylidene fluoride-trifluoroethylene copolymer," J. Appl. Phys. **57**, 5036–5042 (1985).

[40]H. Zhu, S. Pruvost, P. J. Cottinet, and D. Guyomar, "Energy harvesting by nonlinear capacitance variation for a relaxor ferroelectric poly(vinylidene fluoride-trifluoroethylene- chlorofluoroethylene) terpolymer," Appl. Phys. Lett. **98**, 222901 (2011).

[41]M. J. Zehetbauer and Y. T. Zhu, *Bulk Nanostructured Materials* (John Wiley & Sons, 2009).

[42]M. E. Lines and A. M. Glass, *Principles and Applications of Ferroelectrics and Related Materials* (Clarendon Press, Oxford, 1977).

[43]S. B. Lang, "Pyroelectricity: From ancient curiosity to modern imaging tool," Phys. Today **58**, 31–36 (2005).

[44]L. Kouchachvili and M. Ikura, "Improving the efficiency of pyroelectric conversion," Int. J. Energy Res. **32**, 328–335 (2008).

[45]L. Kouchachvili and M. Ikura, "Pyroelectric conversion-effects of P(VDF-TrFE) preconditioning on power conversion," J. Electrostat. **65**, 182–188 (2006).

[46]V. Sencadas, S. Lanceros-Mendez, and J. F. Mano, "Characterization of poled and non-poled b-PVDF films using thermal analysis techniques," Thermochim. Acta **424**, 201–207 (2004).

[47]B. Chu, X. Zhou, K. Ren, B. Neese, M. Lin, Q. Wang, F. Bauer, and Q. M. Zhang, "A dielectric polymer with high electric energy density and fast discharge speed," Science **313**, 334–336 (2006).

[48]G. H. Haertling, "Ferroelectric Ceramics: History technology," J. Am. Ceram. Soc. **82**, 797–818 (1999).

[49]H. Kara, R. Ramesh, R. Stevens, and C. R. Bowen, "Porous PZT ceramics for receiving transducers," IEEE Trans. Ultrason. Ferroelectr. Freq. Control **50**, 3289–3296 (2003).

[50]F. Levassort, J. Hole, E. Ringgaard, T. Bove, M. Kosec, and M. Lethiecq, "Fabrication, modelling use of porous ceramics for ultrasonic transducer applications," J. Electroceram. **19**, 127–139 (2007).

[51]C. R. Bowen, H. A. Kim, P. M. Weaver, and S. Dunn, "Piezoelectric and ferroelectric materials and structures for energy harvesting applications," Energy Environ. Sci. **7**, 25–44 (2014).

[52]C. R. Bowen, J. Taylor, E. LeBoulbar, D. Zabek, A. Chauhan, and R. Vaish, "Pyroelectric materials and devices for energy harvesting applications," Energy Environ. Sci. **7**, 3836–3856 (2014).

[53]Y. Shindo and F. Narita, "Piezomechanics in PZT stack actuators for cryogenic fuel injectors," in *Smart Actuation and Sensing Systems*, edited by G. Berselli, R. Vertechy, and G. Vassura (InTech, Rijeka, 2012), Chap. 24.

[54]Y. Jeong, J. Yoo, S. Lee, and J. Hong, "Piezoelectric characteristics of low temperature sintering Pb(Mn$_{1/3}$Nb$_{2/3}$)O$_3$–Pb(Ni$_{1/3}$Nb$_{2/3}$)O$_3$–Pb(Zr$_{0.50}$Ti$_{0.50}$)O$_3$ according to the addition of CuO and Fe$_2$O$_3$," Sens. Actuators A Phys. **135**, 215–219 (2007).

[55]P. D. Gio, L. D. Vuong, and H. T. T. Hoa, "Electrical properties of CuO-doped PZT–PZN–PMnN piezoelectric ceramics sintered at low temperature," J. Mater. Sci. Chem. Eng. **2**, 20–27 (2014).

[56]C. T. Cheng, C. S. Yuan, H. C. Shong, and C. S. Fang, "Effects of ZnO on the dielectric, conductive and piezoelectric properties of low-temperature-sintered PMnN–PZT based hard piezo-electric ceramics," J. Eur. Ceram. Soc. **31**, 2013–2022 (2011).

[57]D. Dong, M. Xiong, K. Murakami, and S. Kaneko, "Lowering of sintering temperature of Pb(Zr,Ti)O$_3$ ceramics by the addition of BiFeO$_3$ and Ba(Cu$_{0.5}$W$_{0.5}$)O$_3$," Ferroelectrics **145**, 125–133 (1993).

[58]G. A. Smolenskii and A. I. Agranovskaya, "Dielectric polarization of and losses of some complex compounds," Sov. Phys. Tech. Phys. **3**, 1380–1382 (1958).

[59]G. A. Smolenskii, "Physical phenomena in ferroelectrics with diffused phase transition," J. Phys. Soc. Jpn. **28**, 26–37 (1970).

[60]B. Jaffe, R. S. Roth, and S. Marzullo, "Piezoelectric properties of lead zirconate–lead titanate solid-solution ceramics," J. Appl. Phys. **25**, 809–810 (1954).

[61]D. Dong, K. Murakami, S. Kaneko, and M. Xiong, "Piezoelectric properties of PZT ceramics sintered at low temperature with complex-oxide additives," J. Phys. Soc. Jpn. **101**, 1090–1094 (1993).

[62]J. H. Moon, H. M. Jang, and B. D. You, "Densification behaviors and piezoelectric properties of MnO$_2$, SiO$_2$-doped Pb(Ni$_{1/3}$Nb$_{2/3}$)O$_3$–PbTiO$_3$–PbZrO$_3$ ceramics," J. Mater. Res. **8**, 3184–3191 (1993).

[63]J. H. Cho, I. K. Park, H. T. Chung, and H. G. Kim, "The effects of Cd-substitution site on sintering behavior and electrical properties in Pb(Ni$_{1/3}$Nb$_{2/3}$)O$_3$–PbZrO$_3$–PbTiO$_3$ ceramics," Jpn. J. Appl. Phys. **36**, 181–187 (1997).

[64]D. Zabek, J. Taylor, E. L. Boulbar, and C. R. Bowen, "Micropatterning of flexible and free standing polyvinylidene difluoride (PVDF) films for enhanced pyroelectric energy transformation," Adv. Energy Mater. **5**(8), 1401891 (2015).

[65]J. Li, M. Yang, X. Sun, X. Yang, J. Xue, C. Zhu, H. Liu, and Y. Xia, "Micropatterning of the ferroelectric phase in a poly (vinylidene difluoride) film by plasmonic heating with gold nanocages," Angew. Chem. **128**, 14032–14036 (2016).

[66]C. C. Hsiao, J. W. Jhang, and A. S. Siao, "Study on pyroelectric harvesters integrating solar radiation with wind power," Energies **8**, 7465–7477 (2015).

[67]A. S. Siao, C. K. Chao, and C. C. Hsiao, "Study on pyroelectric harvesters with various geometry," Sensors **15**, 19633–19648 (2015).

[68]C. C. Hsiao, J. C. Ciou, A. S. Siao, and C. Y. Lee, "Temperature field analysis for PZT pyroelectric cells for thermal energy harvesting," Sensors **11**, 10458–10473 (2011).

[69]C. C. Hsiao, A. S. Siao, and J. C. Ciou, "Improvement of pyroelectric cells for thermal energy harvesting," Sensors **12**, 534–548 (2012).

[70]C. C. Hsiao and A. S. Siao, "Improving pyroelectric energy harvesting using a sandblast etching technique," Sensors **13**, 12113–12131 (2013).

[71]A. S. Siao, C. K. Chao, and C. C. Hsiao, "A strip cell in pyroelectric devices," Sensors **16**, 375 (2016).

[72]C. C. Hsiao and A. S. Siao, "A high aspect ratio micro-pattern in freestanding bulk pyroelectric cells," Energy Technol. **5**, 1–17 (2017).

[73]H. Bartzsch, D. Glöß, P. Frach, M. Gittner, E. Schultheiß, W. Brode, and J. Hartung, "Electrical insulation properties of sputter-deposited SiO$_2$, Si$_3$N$_4$ and Al$_2$O$_3$ films at room temperature and 400°C," Phys. Status Solidi A **206**, 514–519 (2009).

[74]J. H. Park, H. Kim, D. S. Yoon, S. Y. Kwang, J. Lee, and T. S. Kim, "Effects of the material properties on piezoelectric PZT thick film micro cantilevers as sensors and self actuators," J. Electroceram. **25**, 1–10 (2010).

[75]S. W. Zhou and C. A. Rogers, "Heat generation, temperature, and thermal stress of structurally integrated piezo-actuators," J. Intell. Mater. Syst. Struct. **6**, 372–379 (1995).

[76]W. Albrecht, "How thickness and material properties influence thermal shock stresses in flat plates and cylinders," in *ASME 1969 Gas Turbine Conference and Products Show, March, 1969* (American Society of Mechanical Engineers, 1969), pp. V001T01A076-V001T01A076.

[77]K. Natori, D. Otani, and N. Sano, "Thickness dependence of the effective dielectric constant in a thin film capacitor," Appl. Phys. Lett. **73**, 632–634 (1998).

[78]See http://www.ti.com/lit/ds/sbos148/sbos148.pdf for data sheet for OPA-128.

[79]M.W. Hooker, Properties of PZT-based Piezoelectric Ceramics between −150 and 250°C. NASA/CR-1998-208708 (National Aeronautics and Space Administration, Langley Research Center, 1998).

[80]B. Vodopivec, C. Filipič, A. Levstik, J. Holc, and Z. Kutnjak, "Dielectric properties of partially disordered lanthanum-modified lead zirconate titanate relaxor ferroelectrics," Phys. Rev. B **69**, 224208 (2004).

[81]P. Butnoi, N. Pisitpipathsin, P. Kantha, P. Bintachitt, and K. Pengpa, "Phase transition and dielectric properties of PNNZT-BNLT ceramics," Ferroelectrics **452**, 1–6 (2013).

[82]K. Krishnamurthy, F. Lalande, and C. A. Rogers, "Effects of temperature on the electrical impedance of piezoelectric sensors," Proc. SPIE **2717**, 302–310 (1996).

[83]M. Pavel, I. Rychetský, and J. Petzelt, "Polar clusters in relaxor (Pb, La)(Zr, Ti)O_3 revealed by second harmonic generation," J. Appl. Phys. **89**, 5036–5039 (2001).

[84]S. Pandya, J. Wilbur, J. Kim, R. Gao, A. Dasgupta, C. Dames, and L. W. Martin, "Pyroelectric energy conversion with large energy and power density in relaxor ferroelectric thin films," Nat. Mater. **7**, 432–438 (2018).

[85]R. Moazzami, C. Hu, and W. H. Shepherd, "Electrical characteristics of ferroelectric PZT thin films for DRAM applications," IEEE Trans. Electron Devices **39**, 2044–2049 (1992).

[86]E. A. Skrabek and J. W. McGrew, "*Pioneer 10 and 11 RTG performance update*," in Transactions of the Fourth Symposium on Space Nuclear Power Systems (Sandia National Laboratories, 1987), pp. 201–204.

[87]D. Wang, Y. Fotinich, and G. P. Carman, "Influence of temperature on the electromechanical and fatigue behavior of piezoelectric ceramics," J. Appl. Phys. **83**, 5342–5350 (1998).

[88]H. Cao and A. G. Evans, "Electric-field-induced fatigue crack growth in piezoelectrics," J. Am. Ceram. Soc. **77**, 1783–1786 (1994).

[89]S. H. Krishnan, D. Ezhilarasi, G. Uma, and M. Umapathy, "Pyroelectric-based solar and wind energy harvesting system," IEEE Trans. Sustain. Energy **5**, 73–81 (2014).